Experimental and numerical study of melting in a cylinder

Benjamin J. Jones, Dawei Sun, Shankar Krishnan, Suresh V. Garimella *

*School of Mechanical Engineering, Cooling Technologies Research Center, Purdue University,
585 Purdue Mall, West Lafayette, IN 47907-2088, USA*

Abstract

Well-controlled and well-characterized experimental measurements are obtained during the melting of a moderate-Prandtl-number material (*n*-eicosane) in a cylindrical enclosure heated from the side. The study aims to provide benchmark experimental measurements for validation of numerical codes. Experimental results in terms of measured temperatures and melt front locations are reported in both graphical and tabular forms. The melt front was captured photographically and its location ascertained using digital image processing techniques. To facilitate numerical validation exercises, a complete set of experimental results have been made available on a website for public access. An illustrative numerical comparison exercise was also undertaken using a multiblock finite volume method and the enthalpy method for a range of Stefan numbers. The experimental boundary conditions can be adequately represented with a constant and uniform side wall temperature, a constant and uniform lower surface temperature, and an adiabatic top wall. Very good agreement was obtained between the predictions and the experiment for Stefan numbers of up to 0.1807. The experimental results for a Stefan number of 0.0836 are recommended as being the most suitable for numerical benchmarking, since the boundary conditions are best controlled in this set of experiments.

1. Introduction

Problems involving solid/liquid phase change are encountered in many scientific and engineering applications such as crystal growth [1], latent heat thermal energy storage for thermal control [2,3], casting processes [4], and cryopreservation of cells and tissues [5]. Detailed investigations of the heat and mass transfer processes and solidification and melting mechanisms involved in these applications demand carefully designed and rigorously characterized experiments and advanced numerical modeling techniques. A good review of this subject was compiled by Yao and Prusa [6].

A number of experimental efforts have investigated the solid front evolution and heat and mass transfer characteristics of low-Prandtl-number materials such as gallium and tin. Temperature fields and solid front locations during the solidification of superheated tin in a rectangular cavity were reported by Wolff and Viskanta [7]. A probing technique was employed to detect the location of the solid/liquid interface. Gau and Viskanta [8] investigated melting of gallium from a vertical wall, with reference to the effect of natural convection on the shape and motion of the solid front. The volumetric solid fraction was determined by pouring out the melt at specific times and measuring the remaining solid. Due to the anisotropic nature of the gallium crystals and natural convection effects, the interface morphology was irregular and the shape of the interface was not reproducible [8]. Campbell and Koster [9] reported on a non-intrusive, real-time, radioscopic observation technique to detect the location of the phase-change interface during the melting of gallium from a vertical wall.

Solid–liquid phase change in high-Prandtl-number materials such as paraffin wax and silicone oil has also been

* Corresponding author. Tel.: +1 765 494 5621; fax: +1 765 494 0539.
 E-mail address: sureshg@purdue.edu (S.V. Garimella).

Nomenclature

A	Carman–Kozeny coefficient, Eq. (9)
C	constant, Eq. (9)
c_p	specific heat
D	diameter
f	intensity of an image
f_L	liquid fraction
Fo	Fourier number, $\alpha t/R^2$
g	gravitational vector
h	heat transfer coefficient, linear contrast enhancement
H	height
I	identity tensor
k	thermal conductivity
L	latent heat
M	maximum grayscale value
m	maximum intensity
n	index of refraction
Nu	Nusselt number, hR/k
p	pressure
Pr	Prandtl number, $c_p\mu/k$
q''	heat flux
r	radius, coordinate in the radial direction
R	radius of the inner cylinder
Ra	Rayleigh number, $g\beta(T_H - T_m)R^3/(\alpha v)$
Sc	degree of subcooling $(T_i - T_m)/(T_H - T_m)$
Ste_L	Stefan number, $c_{pL}(T_H - T_m)/L$
t	time, thickness of top acrylic block
T	temperature
Th	intensity threshold

u	velocity vector
V_{melt}	volume of the molten material
V_{total}	total volume of the enclosure
z	coordinate in the vertical direction

Greek symbols

α	thermal diffusivity
β	thermal expansion coefficient
δ	thickness of the polycarbonate wall
ε	artificial mushy zone thickness
θ	non-dimensional temperature $(T - T_m)/(T_H - T_m)$
μ	dynamic viscosity
v	kinematic viscosity
ρ	density
$\bar{\psi}$	stream function
ψ	non-dimensional stream function, $\bar{\psi}/\alpha$

Subscripts

a	actual
B	base
H	side wall
i	initial
∞	ambient
L	liquid
m	melting, measured
ref	reference
S	solid
U	upper

experimentally studied. Ho and Viskanta [10] and Bénard et al. [11] investigated the phase change of *n*-octadecane in a rectangular cavity; the melt front location was determined photographically in both studies due to the transparency of the melt.

A majority of past studies have considered phase change in rectangular cavities and only a few experimental investigations in cylindrical enclosures have been reported. This geometry is important in many practical applications such as casting processes, thermal storage systems, and food processing. The melting behavior of various paraffin waxes in a cylindrical enclosure was investigated experimentally by Bareiss and Beer [12]. The solid–liquid interface location was inferred indirectly by using embedded, closely spaced thermocouples to detect the steep temperature rise associated with the thermal boundary layer as the melt front passed close to a thermocouple. Sparrow and Broadbent studied the freezing [13] and melting [14] of *n*-eicosane in a vertical tube both experimentally and numerically. A pour-out technique was employed in the experiments to measure the solid fraction. Direct visualization of the melt front was conducted by Menon et al. [15], in a transparent test cell heated by a hot water bath. Photographs of the

melt front were obtained and tracer particles used to qualitatively explore the flow patterns.

In addition to experimental investigations, numerical simulations based on either moving or fixed grids have been widely used in the study of solid/liquid phase change problems, facilitated by rapid increases in computational power [16,17]. Variants of the enthalpy method, such as the enthalpy-porosity method [16] and apparent heat capacity method [17] have been employed. Numerical techniques based on moving grids have also been proposed [18,19]. A comparison of fixed and moving grids was performed by Viswanath and Jaluria [20] and later by Bertrand et al. [21]. They found that the appropriate choice in the solution method is often problem-dependent. Therefore, advancements in numerical modeling depend upon validation against rigorously controlled and well-documented experimental results. Experimental data for the melting of gallium and the solidification of tin [7,8] have been employed by various investigators for validating predictions [18,19].

However, comparison against existing experimental results has often yielded less than satisfactory agreement; while global and qualitative agreements have been obtained, detailed quantitative comparisons have not been

possible [21]. Desired boundary conditions are difficult to impose exactly in experiments; at the same time, the boundary conditions that do exist in experiments have not been fully specified in a manner that facilitates incorporation into numerical models. Uncertainties in temperature measurements and melt front descriptions in most of the existing experiments have also resulted in difficulties in proper validation of numerical models. Benchmarking exercises have thus often been limited to numerical results from one approach being compared against numerical results from other sources [17,21]. Conflicting results pertaining to the morphology of the melt front as well as the flow structures and heat transfer characteristics have been reported by different authors [22,23], most notably for tin solidification and gallium melting; such conflicts in the modeling literature are difficult to resolve without the benefit of well-characterized benchmark experiments.

The primary objective of this work was to obtain experimental measurements in a solid/liquid phase change problem with rigorously controlled boundary conditions. The experimental results presented could serve as a basis for validating modeling approaches. Numerical simulations employing the enthalpy method are also conducted, and the results compared against the experimental measurements. The present work also sheds light on transport mechanisms in play during melting in a cylindrical enclosure.

2. Experimental setup and procedures

2.1. Apparatus and instrumentation

A paraffin wax, *n*-eicosane, was chosen as the test material because of its opacity in the solid state combined with

optical clarity in the molten state, lending itself well to visualization of the solid–liquid interface. Also, the relatively low melting point of 36.4 °C [24] for this material facilitated the experiment design. A schematic diagram of the experimental facility is shown in Fig. 1; special care was taken to impose well-characterized and documented boundary conditions in the experiment. A cylindrical enclosure was chosen for this study since it is easier to isolate the heat transfer surfaces from the environment in this case than with a rectangular enclosure. The phase change material (PCM) was introduced into the transparent cylindrical enclosure consisting of a cylindrical shell made of polycarbonate, an acrylic base, and an acrylic block on top. The outer surface of the cylinder was maintained at a constant temperature by immersion in a hot water bath. An immersion-type circulating heater maintained the water in the rectangular polycarbonate bath at a constant, uniform temperature. Due to the low thermal conductivity of the polycarbonate cylinder ($k = 0.19$ W/m K [25]), the temperature on the inner surface of the cylinder varies with time and along the cylinder height. The nearly constant and uniform exterior temperature measurements on the cylinder are therefore recommended for use in numerical models, with the polycarbonate cylinder wall being included in the computational domain.

It is desired that the top of the PCM domain be well insulated. This would allow the melting to be driven by radial heating from the cylinder wall. However, the low thermal conductivity of solid *n*-eicosane ($k = 0.423$ W/m K [26]) and the need for transparency of the upper test vessel material to facilitate illumination of the melt front render typical insulation materials unsuitable. As a result, the top wall was made from a thick block of acrylic
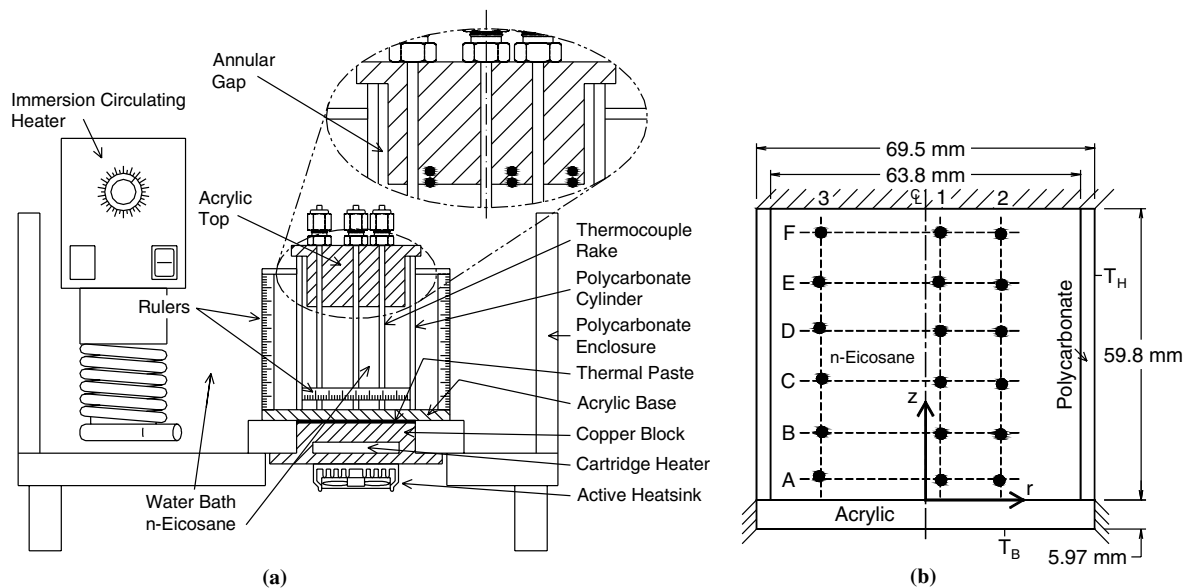
Fig. 1. (a) Schematic diagram of the experimental facility, and (b) cylindrical enclosure dimensions and boundary conditions. Inset in (a) shows an expanded view of the top of the test cell and the locations of the thermocouples imbedded in the acrylic top. The thermocouples are approximately 0.5 mm and 3.8 mm from the lower surface of the acrylic top. An enlarged view of the test cylinder is shown in (b). The polycarbonate side wall is at a constant temperature T_H on the outside, the acrylic bottom wall is at a constant temperature T_B on the outside, and the top wall is adiabatic. The radial edge of the acrylic bottom wall is insulated as shown.

($k = 0.193$ W/m K [27]). Since the conductivities of the PCM and top wall are comparable, heat conduction to the surroundings through the top wall is non-negligible. This heat flow was reduced by use of a thick wall ($t = 41$ mm), and calculated using temperature readings from thermocouples mounted at different locations in the top wall as shown in the inset of Fig. 1a. It was determined that no more than 5% of the total energy gained by the PCM during the course of each experiment is transferred through the top wall. Thus, an adiabatic boundary condition may be assumed at the top of the PCM domain in a numerical model of the problem.

A narrow annular gap between the acrylic top and the polycarbonate cylinder provides accommodation for the expanding PCM as it melts (see Fig. 1a). The excess wax was periodically siphoned from the annular gap using a syringe to prevent the wax from eventually solidifying at the top of the gap. The volume of wax siphoned was about 8% of the initial volume. The level of the wax was maintained approximately 1–2 mm above the bottom surface of the acrylic top by this process, so as to avoid the formation of a free surface in the domain (which would have invalidated the boundary condition for the top surface of the domain).

Insulated conditions could not be achieved on the lower wall of the PCM domain due to difficulties with isolating the heat leakage from the lower wall while immersed in the hot water bath. Instead, a known temperature boundary condition was imposed on the outside of an acrylic base. The desired constant surface temperature condition on the bottom surface of the acrylic base was achieved by controlling the temperature of a large copper block pressed against the acrylic base with a thin layer of thermally conductive paste (see Fig. 1a). Heating was achieved by means of an embedded 150 W cartridge heater in the copper block, while cooling was accomplished via the use of a fan-cooled heat sink attached to the bottom of the copper block. The desired temperature was set by controlling the power input to the cartridge heater with a PID temperature controller, while the fans on the heat sink were operated at full power. A T-type thermocouple located on the bottom surface of the acrylic base served as the input to the temperature controller. The acrylic base would need to be included in a numerical model of the domain, with the uniform and constant temperature on its outside being known.

Fig. 1b shows the dimensions of the phase change enclosure and the imposed boundary conditions: T_H is the temperature imposed on the exterior side wall of the enclosure while T_B is the temperature of the lower surface of the acrylic base. Only a portion of the acrylic base is shown in Fig. 1b. The acrylic base extends to a large outer diameter of 120.7 mm and serves as a flange by which to mount the enclosure to the water tank; an insulated condition is assumed at the radius of $r = 34.75$ mm as shown in the simplified geometry in Fig. 1b. This assumption will be shown to be valid later in this paper (Section 4.2.1).

All temperatures were measured using 36-gauge, T-type thermocouples. The estimated uncertainty in the temperature measurements is ±1.4 °C while the resolution of the data acquisition system is 0.008 °C. Three thermocouple rakes, constructed from 3.2 mm outer-diameter plastic tubing, were placed vertically in the PCM domain at three different radial locations. Each rake contained six evenly spaced thermocouples. The relative positions and labeling convention of the thermocouples are shown in Fig. 1b; the measured locations of the thermocouples from which results are presented in this paper are provided in Table 1. Thermocouples were attached to the exterior cylindrical shell at several locations to verify the uniformity of the temperature boundary condition; the temperature on this surface was found to be uniform to within 0.5 °C. Three thermocouples placed along the bottom of the acrylic base showed the lower boundary temperature to be uniform to within 0.7 °C. The good control of temperatures in the setup allowed for the average side and lower boundary temperatures to be maintained to within ±0.3 °C of the desired values.

The melt front locations were captured using digital photography. While the refractive index of the water in the bath ($n = 1.33$) is comparable to that of the *n*-eicosane melt ($n = 1.435$ at 40 °C [28]), some distortion of the visualized melt front still occurs due to refraction effects. The cylindrical geometry of the enclosure causes a noticeable distortion in the radial (r) direction, while the vertical (z) direction remains largely unaffected. The melt front location could therefore be measured using a horizontal ruler located inside the cylinder in conjunction with the vertical rulers located on each side of the cylindrical enclosure as shown in Fig. 1a. However, using the rulers to manually measure the locations of the melt front is laborious and, as will be discussed in more detail in Section 2.3, a more automated approach that is easily implemented into digital image processing techniques is desirable. Using geometric optics, a relationship between measured radial location (r_m) from the digital images and the actual radial location (r_a) of the solid/liquid interface can be derived (see Fig. 2):

$$r_a = \frac{n_1}{n_2} r_m \tag{1}$$

Table 1
Measured locations of thermocouples from which results are presented in this paper

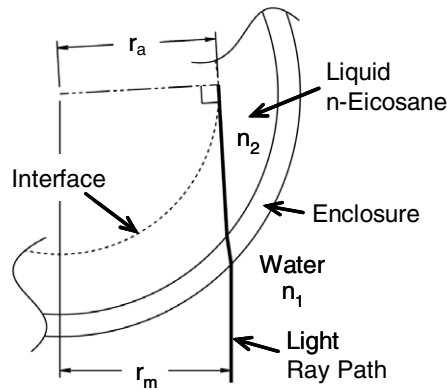|	A1	B1	C1	D1	E1	F1	A3	B3	C3	D3	E3	F3
r (mm)	3.2	3.2	3.1	3.1	2.7	3.1	21.9	21.3	21.3	21.8	21.9	21.5
z (mm)	4.1	13.6	24.2	34.7	44.8	54.9	4.9	14.0	24.9	35.3	44.8	54.9

Fig. 2. Geometric construction of light ray path to melt front.

where n_1 and n_2 are the indices of refraction of the water and the liquid n-eicosane, respectively. Eq. (1) is used to correct for the radial distortion in the digital images while the rulers only served to verify the results.

2.2. Experimental procedure

Melted wax was injected into the cylindrical enclosure using a syringe and allowed to solidify. To avoid the large voids that formed if the entire domain was filled and allowed to solidify in one step, the melt was added and allowed to solidify in layers that were approximately 4 mm thick instead. Each layer was allowed to solidify and cool for approximately 40–60 min before another layer was added. After filling the enclosure, the wax was allowed to equalize to ambient temperature ($T_i \approx 23\,°C$), which is the initial temperature for the experiments.

At the start of the experiment, hot water was quickly poured into the tank, power was supplied to the cartridge heater, and the heat sink fans were turned on. The immersion heater maintained the water bath at the desired temperature and the temperature controller maintained the power level of the cartridge heater. Temperature readings were recorded at 15 s intervals. Photographs of the melt front were recorded every 1–4 min, depending on the total duration of the experiment; approximately 70 photographs were obtained for each experiment. Three sets of experiments were performed with varying sidewall temperatures as shown in Table 2. The experiments for wall temperatures of 70 and 55 °C were each performed twice to verify repeatability. The time required to reach a liquid fraction (V_{melt}/V_{total}) of 0.85 in the two 70 °C experiments differed

Table 2
Experimental conditions for the three cases investigated

	Case I	Case II	Case III
Side wall temperature, T_H (°C)	70	55	45
Lower surface temperature, T_B (°C)	32	32	32
Rayleigh number, Ra	2.75×10^7	1.31×10^7	5.45×10^6
Stefan number, Ste_L	0.3265	0.1807	0.0836

by 1.8% [$(SteFo)_L = 0.0761$ and 0.0775]; in the 55 °C experiments, this difference was only 0.13% [$(SteFo)_L = 0.0765$ and 0.0766].

2.3. Image analysis and melt front tracking

The location and shape of the phase-change interface was extracted from the digital images acquired during the experiments using edge-detection algorithms in MATLAB [29]. Identification of the interface was enabled by the solid wax being opaque while the melt is transparent, but was complicated by the presence of the cylinder wall, thermocouple rakes, air bubbles and non-uniform illumination in the images. The image quality was improved using contrast enhancement, intensity thresholding, and filtering operations, so that the edge of the solid region could be more easily detected. For example, some of the background features were removed by subtracting an image of the interface from an image at a later time. If $f_{t_0}(x, y)$ represents the intensity of an image at time t_0 and $f_{t_0+\Delta t}(x, y)$ represents the intensity of an image after a time interval of Δt, the image resulting from subtraction is described by

$$g_{t_0}(x, y) = f_{t_0}(x, y) - f_{t_0+\Delta t}(x, y) \tag{2}$$

The net result is an image that highlights only the features that change between $t_0 + \Delta t$ and t_0. The result of a sample subtraction operation, shown in Fig. 3b, still suffers from poor contrast and non-uniform illumination. These issues were addressed by applying linear contrast enhancement to different regions along the height of the image with the intensity in region i given by $g_{t_0}^i(x, y)$. If m^i is the maximum intensity in region i and M is the maximum grayscale value, the linear contrast enhancement is described by

$$h_{t_0}^i(x, y) = \frac{M}{m^i} g_{t_0}^i(x, y) \tag{3}$$

A threshold was used to remove all of the low-intensity pixel values. If Th represents the threshold intensity value, this operation is described by

$$\begin{aligned} &\text{If } h_{t_0}(x, y) < Th, \text{ then } z_{t_0}(x, y) = 0 \\ &\text{If } h_{t_0}(x, y) > Th, \text{ then } z_{t_0}(x, y) = h_{t_0}(x, y) \end{aligned} \tag{4}$$

The threshold value was manually adjusted until a good compromise was achieved between attenuation of low-intensity noise and retention of original detail.

A 10×10 median filter was employed to smooth out the remaining noise and artifacts. The edge detection employed a gradient-based method by implementing Robert's approximation for the derivative. This method sets the pixel value to maximum intensity at the locations where the gradient is a local maximum [30]. Fig. 3c shows the edges that were detected in the image shown in Fig. 3b. The interface location at time t_0 is the outer edge in Fig. 3c. Since this was the edge of interest, all other edges were therefore removed.

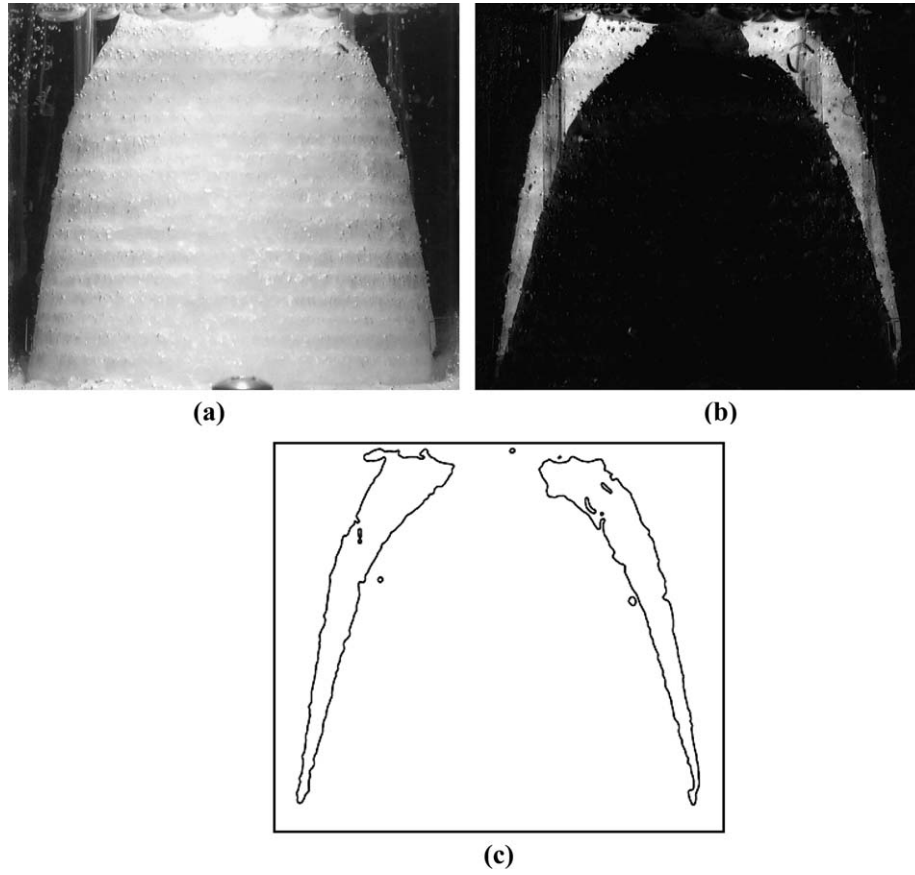The actual position of the interface in object space was then determined from a knowledge of the image-to-object

Fig. 3. Image processing to determine interface location. (a) Original image captured during melting process with a wall temperature of $T_H = 70\ °C$ at a time $t_0 = 1260$ s. (b) Image resulting from a subtraction of the image in (a) by an image at a time of $t_0 + \Delta t = 1740$ s. (c) Edges detected after further image processing.

dimensional ratio, which was found by comparing the known outer diameter of the cylindrical enclosure to the number of pixels this distance occupies in the image. Due to distortion of the images in the radial direction by refraction, the radial position of the interface must be corrected using Eq. (1).

3. Numerical analysis

3.1. Mathematical formulation

The governing equations for an incompressible fluid in an axisymmetric domain can be written as

$$\nabla \cdot (\rho \underset{\sim}{u}) = 0 \tag{5}$$

$$\frac{\partial(\rho \underset{\sim}{u})}{\partial t} + \nabla \cdot (\rho \underset{\sim}{u}\, \underset{\sim}{u}) = -\nabla p + \nabla \cdot (\mu \nabla \underset{\sim}{u})$$
$$+ \rho_\infty [1 - \beta(T - T_{ref})] \underset{\sim}{g} + \underset{\approx}{A}\, \underset{\sim}{u} \tag{6}$$

$$\rho \left(c_p + \frac{\partial f_L}{\partial T} L \right) \frac{\partial T}{\partial t} + \nabla \cdot (\rho \underset{\sim}{u} T) = \nabla \cdot (k \nabla T) \tag{7}$$

The buoyancy effects in the momentum equations are modeled using the Boussinesq approximation with T_{ref} as the reference temperature and β the thermal expansion coeffi-

cient. The apparent heat capacity formulation of the enthalpy method is adopted to account for solid/liquid phase change in the domain, in which the contribution of the latent heat to the energy equation is captured as an added heat capacity. In the current implementation, a simple direct evaluation approach [17] is adopted for $\partial f_L/\partial T$ in Eq. (7). The liquid fraction (f_L) is defined as follows:

$$f_L = \begin{cases} 0 & \text{for } T < T_m - \varepsilon/2 \\ \frac{T - T_m + \varepsilon/2}{\varepsilon} & \text{for } |T - T_m| \leqslant \varepsilon/2 \\ 1 & \text{for } T > T_m + \varepsilon/2 \end{cases} \tag{8}$$

in which ε is an arbitrary thickness assigned for the mushy zone representing the interface between the solid and liquid regions. The solution of the energy equation is not sensitive to the assumed variation of f_L with temperature if ε is relatively small. For all the computations performed in this study, ε was fixed at 0.1 K.

In order to model the flow in the mushy zone where $0 < f_L < 1$, Darcy's law with an isotropic resistance tensor based on the Carman–Kozeny equation is adopted

$$\underset{\approx}{A} = C \frac{(1 - f_L)^2}{f_L^3} \underset{\approx}{I} \tag{9}$$

in which $\underset{\approx}{I}$ is the identity matrix and C is a constant [17].

Table 3
Thermophysical properties of n-eicosane [24,26,31,32]

	Solid (25 °C)	Liquid (50 °C)
Density ρ (kg/m^3)	910	769
Thermal conductivity k (W/m K)	0.423	0.146
Specific heat c_p (J/kg K)	1926	2400
Thermal expansion coefficient β (1/K)	N/A	8.161×10^{-4}
Reference temperature T_{ref} (°C)	N/A	36.4
Melting point T_m (°C)	36.4	
Latent heat L (kJ/kg)	248	

3.2. Implementation

Thermophysical properties of n-eicosane listed in Table 3 [24,26,31,32] were assumed to be temperature-invariant, except for the viscosity of n-eicosane, which is a strong function of temperature, as represented by [31]

$$\log_{10}\mu = -9.2095 + 1822.1/T + 1.6798 \times 10^{-2}T$$
$$- 1.2861 \times 10^{-5}T^2 \quad \text{for } 310 \leqslant T \leqslant 767 \quad (10)$$

The dynamic viscosity (μ) in Eq. (10) is in units of cP, while the temperature (T) is in K. At $T = 50$ °C, the Prandtl number of n-eicosane is $Pr = 53.7$. Since the volumetric expansion of the wax during phase change was not modeled in the numerical simulation, an average value of solid and liquid densities was used. The properties used for the polycarbonate enclosure and acrylic base are listed in Table 4 [25,27,33].

As discussed earlier, the polycarbonate cylinder and acrylic base must be included in a conjugate analysis in the numerical model to properly represent the experimentally measured boundary conditions, where the outside of the cylinder is at a constant temperature T_H, the bottom of the acrylic base is at a constant temperature T_B, and the top is treated as adiabatic (see Fig. 1b and Table 2 for complete details). The conjugate heat transfer problem, including the solid/liquid phase change described by Eqs. (5)–(7), is solved using the SIMPLE algorithm based on a finite volume method [34]. A second-order implicit discretization scheme is used for the transient terms while the convective terms are discretized using a second-order upwind scheme with deferred correction. Time steps of 0.1, 0.05, and 0.02 s were used for $Ste_L = 0.0836$, 0.1807, and 0.3265, respectively. Central differencing is adopted for the diffusive terms. A full description of the discretization methods employed in this work is provided in [34]. A conservative, non-conformal multiblock method is employed for the computational domain so that different mesh densities can be used in the solid and liquid regions. Different

Table 4
Thermophysical properties of experimental facility materials [25,27,33]

	Density (kg/m^3)	Thermal conductivity (W/m K)	Specific heat (J/kg K)
Polycarbonate	1200	0.19	1260
Acrylic	1188	0.193	1420

blocks are used for the PCM, acrylic base, and polycarbonate wall. Structured grids are generated within each block independently. A geometric multigrid method is also implemented in the present work to alleviate the numerical inefficiencies introduced by the multiblock approach; further details are available in [1,34].

Grid independence was established using three sets of successively refined meshes (coarse, moderate, and fine). The deviation in temperature, liquid fraction, maximum velocity, and $|\psi|_{max}$ between the moderate and fine grids is 0.1%, 0.24%, 0.05% and 1.68%, respectively, indicating that the moderate grid was sufficient for analyzing the present problem. Therefore, the moderate grid (PCM: 150×80[1]; acrylic base: 20×60; polycarbonate wall: 120×10) is used in the present work.

4. Results and discussion

4.1. Experimental results

Digital photographs of the melting process at four different times for a side wall temperature T_H of 45 °C are shown in Fig. 4. The layered structure apparent in the solid PCM is caused by the layered solidification procedure adopted (Section 2.2). Due to the different solubility of gas in liquid and solid n-eicosane, gas bubbles tend to nucleate along the solid/liquid interface and become entrapped in the solid phase upon solidification [35]. As the wax melted, the entrapped gas bubbles were released and collected at the top of the enclosure (Fig. 4c–d). Although a vacuum could have been used to evacuate gas from the wax, dealing with the higher volumetric void fraction of the n-eicosane [26] in that case would have introduced further difficulties since the voids are not modeled numerically. However, the trapped gas at the top of the enclosure may result in some discrepancy between the experimental and numerical results, especially for higher Rayleigh numbers, since a no-slip boundary condition is used in the model.

It has been shown through a scaling analysis [36] that four distinct regimes occur during melting of fluids with $Pr > 1$ in a rectangular enclosure: (1) pure conduction, (2) mixed convection/conduction, (3) convection dominant, and (4) "shrinking solid". Although the analysis in [36] was developed for a rectangular enclosure heated from the side, similar regimes were observed with the cylindrical enclosure considered in the present study.

Initially, the molten layer thickness is nearly uniform along the z-direction as seen in Fig. 4a. Since the molten layer thickness is very small, conduction is likely to be the dominant heat transfer mechanism. The melt front shape is similar to the pure conduction regime in rectangular enclosures. As the melting progresses, the molten layer thickness begins to vary along the z-direction, with the molten layer being thickest at the top of the enclosure as

---

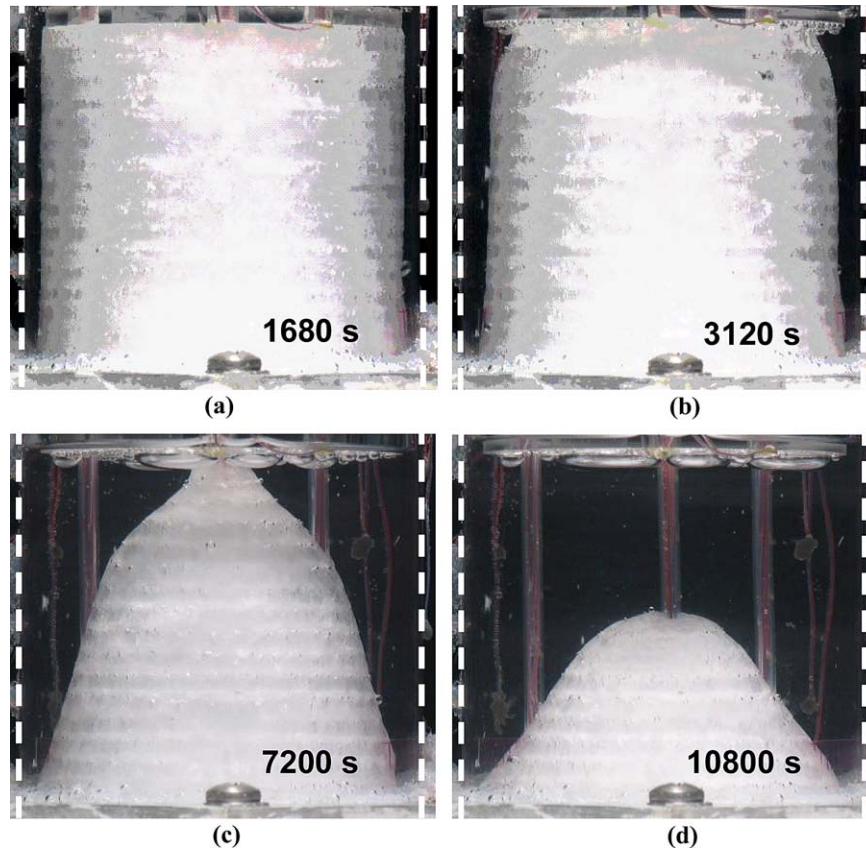[1] Number of grids in z- and r-directions, respectively.

Fig. 4. Photographs during the melting of wax within the cylindrical enclosure for a wall temperature of 45 °C at four different times: (a) 1680 s, (b) 3120 s, (c) 7200 s, and (d) 10,800 s. The solid *n*-eicosane is opaque while the liquid *n*-eicosane is transparent. Also seen in photographs (c) and (d) are the vertically oriented thermocouple rakes. The dashed vertical lines indicate the location of the outside cylinder wall.

observed in Fig. 4b. This indicates that buoyancy-driven natural convection currents are beginning to strengthen, carrying hot liquid toward the top of the enclosure. However, the melt layer thickness is still nearly uniform over much of the cylinder height, which suggests that conduction is still an important mechanism. The appearance of the melt front shape is similar to the mixed convection/conduction regime in [36].

As natural convection currents get established, their effects on the solid/liquid interface become more pronounced. Eventually, the melt layer thickness varies continuously along the height of the cylinder as seen in Fig. 4c. Fig. 4d shows a photograph of the PCM further along in the melting process. By this time, the top portion of the PCM has completely melted away. Fig. 4c and d exhibits melt front shapes similar in appearance to the convection dominant and "shrinking solid" regimes, respectively [36].

Fig. 5 shows temperature profiles along the *z*-direction at two different radial locations corresponding to the A3–F3 thermocouples near the outer wall (Fig. 5a and c) and the A1–F1 thermocouples near the centerline (Fig. 5b and d). The temperatures in Fig. 5a and b are shown for a time when the melting is in its very early stage, with both rakes measuring the temperature of the solid wax. Since the heat transfer in both the liquid and the subcooled solid is governed by conduction, the Fourier number, Fo_S, is the

appropriate time scale during this period. The degree of subcooling is represented in non-dimensional terms as $Sc = (T_i - T_m)/(T_H - T_m)$. In the present study, since all three cases have the same initial temperature, $T_i \approx 23$ °C, the larger the Stefan number, the smaller is the degree of subcooling, i.e., the smaller is the effect of subcooling on the melting process.

In Fig. 5a, the temperatures of the solid PCM are nearly uniform at a radial position near the outside of the enclosure, which indicates a uniform heat flow into the PCM domain along the side wall. This further demonstrates that convection does not play an important role very early in the melt process. At a radial location near the centerline (Fig. 5b), the temperatures are fairly uniform except near the lower surface of the enclosure. This is due to the penetration of heat through the lower surface as a result of the imposed boundary condition on the bottom wall, $T_B = 32$ °C (or $\theta_B/Sc = 0.328$).

Fig. 5c and d shows the temperature profiles at later times (results at three times are shown for each Ste_L), when a substantial portion of the PCM has melted. Since almost all thermocouples are in the liquid region where convective heat transfer is dominant, $\theta = (T - T_m)/(T_H - T_m)$ is used as the non-dimensional temperature and $(SteFo)_L$ is assumed to be the appropriate time scale. The large temperature increase along the *z*-direction at $\theta = 0$ indicates
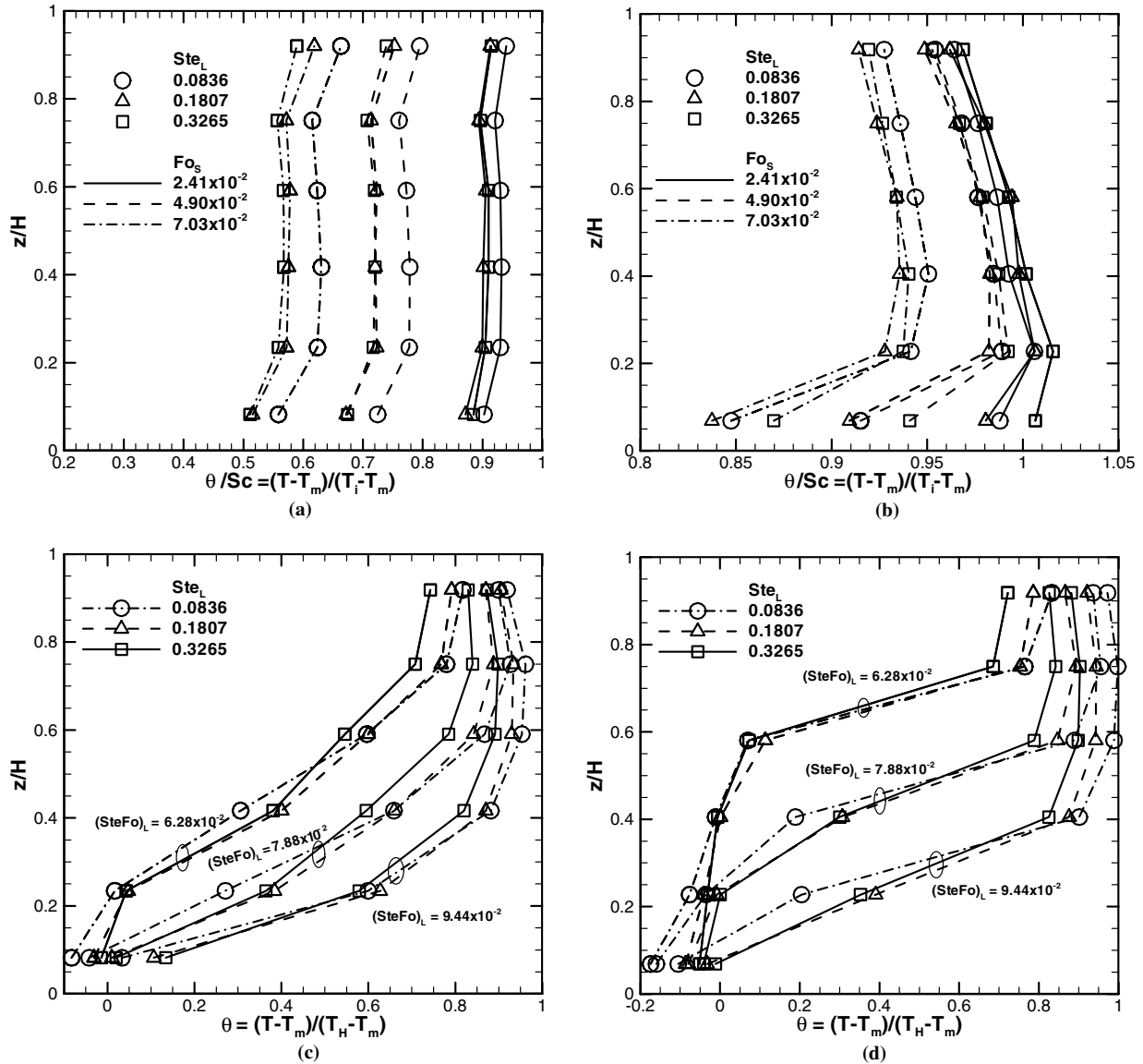
Fig. 5. Temperature profiles corresponding to the (a) A3–F3 and (b) A1–F1 thermocouple locations at early times and to the (c) A3–F3 and (d) A1–F1 thermocouple locations at later times in the melting process.

the presence of the thermal boundary layer close to the solid/liquid interface whereas the sharp temperature gradient near $z/H \sim 1$ is due to the accumulation of hot melt at the top of the enclosure. The liquid PCM temperature near the top of the enclosure approaches that of the side wall, T_H (or $\theta_H = 1$), due to upward heat transport from the side wall by buoyancy-driven convection. At later times, a small drop in temperature is observed near the top of the enclosure, reflecting heat loss through the top.

Tabulated results for the experimentally determined melt front locations and temperatures are presented in Tables 5 and 6, respectively.[2]

4.2. Numerical predictions

The numerical results help in further analyzing and interpreting the experimental measurements of the heat transfer characteristics of the melting process, as discussed below in Section 4.2.2. First, the model is validated and the assumed boundary conditions are evaluated.

4.2.1. Comparison with experiments

In Fig. 6a, the numerically and experimentally determined melt front locations are compared for three different Stefan numbers at selected $(SteFo)_L$ during the melting process. As discussed in Section 2.3, the experimentally determined interface locations were extracted from the digitally processed images. The agreement between the numerical and experimental interface shapes and locations is quite good, especially for lower $(SteFo)_L$. The numerical

---

[2] A complete and detailed database of all the experimental results will remain available at www.ecn.purdue.edu/solidification for the convenience of readers interested in benchmarking exercises.

Table 5
Melt front locations at different times for different Stefan numbers

$Ste_L = 0.0836$						$Ste_L = 0.1807$						$Ste_L = 0.3265$					
2164 s		6964 s		11524 s		1083 s		3243 s		5403 s		603 s		1803 s		3003 s	
r	z	r	z	r	z	r	z	r	z	r	z	r	z	r	z	r	z
27.18	59.46	6.51	57.05	4.34	27.04	26.66	57.64	2.62	56.17	3.20	26.19	27.39	55.91	4.31	56.82	0.51	25.87
28.39	57.25	7.21	55.05	8.04	26.07	27.43	55.55	4.94	54.15	6.30	25.35	27.72	53.69	4.50	54.67	5.92	24.90
28.84	55.05	8.93	53.05	9.57	25.11	28.08	53.45	7.66	52.13	7.79	24.52	28.23	51.47	5.34	52.52	7.40	23.93
28.96	52.85	10.59	51.06	10.72	24.15	28.40	51.36	10.37	50.11	8.63	23.68	28.23	49.25	8.73	50.36	8.87	22.96
28.90	50.65	12.50	49.06	11.80	23.18	28.40	49.27	12.25	48.09	9.79	22.84	28.36	47.03	12.09	48.21	10.61	21.99
28.96	48.44	14.03	47.07	12.70	22.22	28.60	47.18	13.99	46.06	10.89	22.01	27.97	44.81	13.76	46.06	11.57	21.02
28.96	46.24	15.37	45.07	13.52	21.25	28.02	45.09	15.22	44.04	11.67	21.17	28.55	42.59	15.11	43.91	12.48	20.04
29.03	44.04	17.42	43.07	14.23	20.29	28.92	43.00	17.16	42.02	12.51	20.33	28.87	40.37	16.20	41.76	13.44	19.07
28.96	41.83	18.76	41.08	14.80	19.33	28.21	40.90	18.26	40.00	13.22	19.50	28.55	38.15	17.62	39.61	14.28	18.10
29.09	39.63	19.46	39.08	15.25	18.36	28.21	38.81	18.97	37.97	13.99	18.66	29.00	35.93	18.52	37.46	14.85	17.13
28.96	37.43	20.10	37.09	16.08	17.40	28.73	36.72	19.81	35.95	14.51	17.82	28.87	33.71	19.61	35.31	15.43	16.16
28.96	35.23	20.73	35.09	16.97	16.44	28.60	34.63	20.65	33.93	14.90	16.99	28.94	31.49	20.51	33.16	16.08	15.19
29.03	33.02	21.56	33.09	18.18	15.47	28.79	32.54	21.29	31.91	15.35	16.15	28.62	29.27	21.16	31.01	17.36	14.22
29.03	30.82	21.95	31.10	18.95	14.51	28.79	30.44	22.07	29.89	15.74	15.31	28.94	27.05	21.86	28.86	18.13	13.25
28.96	28.62	22.52	29.10	19.84	13.55	28.92	28.35	22.59	27.86	16.51	14.48	29.07	24.83	22.57	26.71	18.97	12.27
29.03	26.42	22.97	27.11	20.67	12.58	28.92	26.26	23.10	25.84	18.00	13.64	29.32	22.61	23.02	24.55	19.61	11.30
28.90	24.21	23.29	25.11	21.56	11.62	28.86	24.17	23.36	23.82	18.77	12.80	28.94	20.39	23.47	22.40	20.13	10.33
28.96	22.01	23.80	23.11	22.39	10.65	28.79	22.08	23.88	21.80	19.55	11.97	29.39	18.17	24.31	20.25	20.71	9.36
28.84	19.81	24.11	21.12	23.16	9.69	28.99	19.98	24.40	19.78	20.33	11.13	29.13	15.95	24.82	18.10	21.35	8.39
28.77	17.61	24.75	19.12	23.99	8.73	29.05	17.89	24.78	17.75	20.91	10.29	29.32	13.73	25.79	15.95	22.06	7.42
28.96	15.40	25.84	17.12	25.01	7.76	29.05	15.80	25.43	15.73	21.62	9.46	29.71	11.51	26.30	13.80	22.76	6.45
29.41	13.20	25.77	15.13	25.77	6.80	29.18	13.71	25.95	13.71	22.39	8.62	29.52	9.29	26.81	11.65	24.05	5.47
29.54	11.00	26.22	13.13	26.16	5.84	29.31	11.62	26.72	11.69	23.04	7.78	29.58	7.07	27.46	9.50	24.44	4.50
29.73	8.80	27.05	11.14	27.05	4.87	29.44	9.53	26.92	9.66	23.56	6.95	28.94	4.85	28.10	7.35	24.69	3.53
29.79	6.59	27.62	9.14	27.56	3.91	29.44	7.43	27.69	7.64	24.07	6.11	28.94	2.63	27.59	5.20	25.59	2.56

Note: All locations are measured in mm. See Fig. 1b for the location of coordinate system.

Table 6
Measured temperature values at selected locations at different times for different Stefan numbers

$Ste_L = 0.0836$						$Ste_L = 0.1807$						$Ste_L = 0.3265$					
t	B1	D1	F1	B3	D3	F3	t	B1	D1	F1	B3	D3	F3	t	B1	D1	F1	B3	D3	F3
726	28.6	28.1	27.4	32.2	32.0	31.1	366	25.1	24.9	25.0	29.8	29.6	29.0	185	22.9	23.0	23.4	26.3	26.2	26.0
1446	33.1	33.0	32.1	34.7	34.6	33.9	726	29.4	29.0	28.3	33.0	32.8	32.0	365	24.5	24.4	24.5	29.8	29.5	29.2
2166	34.6	34.8	34.4	35.4	35.4	35.2	1086	32.1	31.9	31.1	34.4	34.3	34.0	545	26.9	26.5	26.3	31.9	31.6	31.7
2886	35.1	35.6	35.5	35.7	35.7	35.8	1446	33.6	33.7	33.3	35.1	35.1	35.3	725	29.1	28.7	28.3	33.2	33.0	33.7
3606	35.3	35.8	36.0	35.8	35.9	36.1	1806	34.4	34.7	34.8	35.5	35.6	37.7	905	30.8	30.5	30.2	34.1	34.1	36.1
4326	35.5	36.0	36.3	35.9	36.0	38.7	2166	34.8	35.3	35.8	35.7	35.9	44.6	1085	32.0	32.0	32.1	34.7	35.0	46.1
5046	35.6	36.1	36.4	36.0	36.2	40.8	2526	35.0	35.6	36.3	35.8	36.5	46.3	1265	33.0	33.3	33.8	35.1	35.8	51.7
5766	35.6	36.2	36.6	36.0	36.4	41.4	2886	35.3	35.9	36.5	35.9	37.5	47.3	1445	33.7	34.2	35.2	35.4	36.8	53.5
6486	35.6	36.2	36.7	36.1	37.0	41.8	3246	35.4	36.1	38.1	36.0	40.4	48.2	1625	34.2	34.9	36.1	35.7	38.6	54.8
7206	35.6	36.3	36.9	36.1	38.3	42.2	3606	35.5	36.5	48.5	36.2	45.0	49.4	1805	34.5	35.3	36.6	35.9	43.7	56.1
7926	35.7	36.4	42.3	36.2	40.3	42.7	3966	35.5	37.1	49.9	36.6	46.2	50.4	1985	34.8	36.0	54.6	36.2	50.7	57.8
8646	35.7	36.6	43.1	36.4	41.1	43.1	4326	35.7	38.6	51.0	37.3	47.6	51.1	2165	35.0	36.9	58.0	36.8	52.2	59.2
9366	35.8	37.2	43.6	36.6	41.7	43.5	4686	35.8	46.9	51.7	38.7	49.4	51.7	2345	35.3	38.6	59.8	37.8	54.3	60.8
10,086	35.8	38.5	44.1	37.0	42.4	43.8	5046	35.9	51.0	52.3	40.7	51.1	52.2	2525	35.5	42.4	61.5	39.7	56.8	61.8
10,806	35.9	43.3	44.2	37.7	43.3	44.0	5406	36.3	52.2	52.7	43.6	52.1	52.6	2705	35.7	59.1	62.6	42.7	59.5	62.9
11,526	36.1	44.1	44.5	38.7	43.9	44.1	5766	37.0	53.1	53.0	45.1	52.8	52.8	2885	36.1	61.7	63.4	47.3	61.9	63.8
12,246	36.4	44.5	44.7	40.0	44.2	44.2	6126	38.6	53.6	53.4	46.5	53.3	53.1	3065	36.7	63.7	64.3	49.8	63.6	64.4
12,966	36.8	44.8	44.7	40.9	44.5	44.3	6486	44.0	53.9	53.5	48.1	53.7	53.2	3245	38.0	65.0	65.0	51.5	64.8	65.0
13,686	37.9	44.9	44.8	41.5	44.6	44.3	6846	49.5	54.1	53.6	49.6	53.9	53.3	3425	41.1	66.0	65.5	53.9	65.8	65.5
14,406	40.5	44.9	44.8	42.0	44.6	44.3	7206	50.7	54.3	53.7	50.8	54.0	53.4	3605	52.7	66.7	66.4	56.6	66.5	65.6
15,126	42.5	45.0	44.8	42.6	44.7	44.3	7566	51.5	54.5	53.9	51.6	54.2	53.5	3785	59.0	67.2	66.3	59.2	67.0	66.0
15,846	43.1	45.0	44.8	43.0	44.7	44.3	7926	52.1	54.5	53.9	52.2	54.2	53.5	3965	60.9	67.6	66.7	61.3	67.4	66.3
16,566	43.3	45.0	44.8	43.3	44.7	44.3	8286	52.5	54.6	54.0	52.6	54.3	53.6	4145	62.4	67.8	66.9	62.8	67.6	66.5
17,286	43.5	45.0	44.8	43.5	44.7	44.3	8646	52.8	54.6	54.0	52.9	54.4	53.6	4325	63.7	68.0	66.9	63.9	67.9	66.6
18,006	43.7	45.1	44.8	43.7	44.8	44.4	9006	53.1	54.6	53.9	53.1	54.4	53.6	4505	64.6	68.3	67.4	64.8	68.1	66.9

Note: Time (t) is measured in seconds and temperature is measured in °C. B1, D1, F1, B3, D3, and F3 refer to the thermocouple locations. Refer to Fig. 1b for the relative locations of the thermocouples and Table 1 for the measured position of the thermocouples.

results indicate a slightly slower melting rate than what was observed experimentally, resulting in a small deviation between the predicted and experimental melt front locations at the higher $(SteFo)_L$.

The comparison of the numerical and experimental liquid melt volume fractions is shown in Fig. 6b. The liquid melt volume fraction was determined experimentally from the reconstructed interface locations. The experimental and numerical results are again in good agreement. However, consistent with the comparison in Fig. 6a, the numerical results yield a slightly lower liquid fraction than observed in the experiments, particularly at higher $(SteFo)_L$.
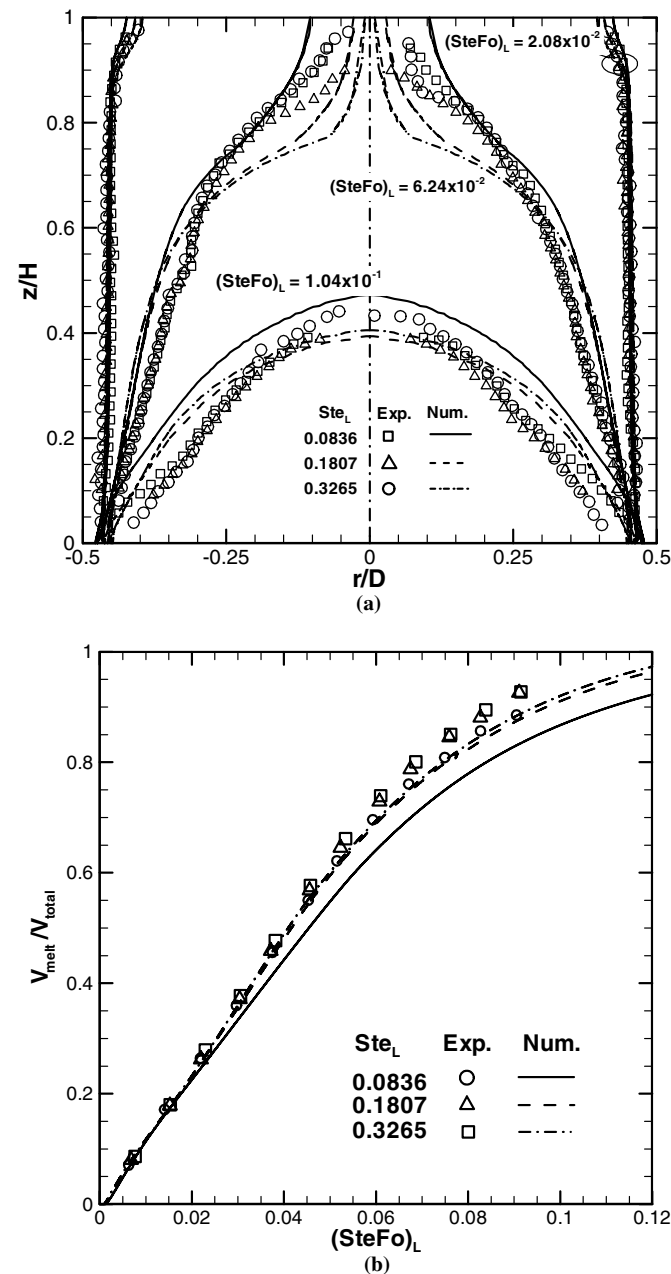
Fig. 7 shows the numerically predicted and experimentally measured temperatures at selected thermocouple locations for the entire duration of the experiments. Initially, the PCM is subcooled and the solid PCM is heated through conduction until the melting temperature is reached. A rapid increase in temperature is observed as the thermal boundary layer associated with the melt front passes by each thermocouple. Eventually, the temperature of the liquid PCM approaches $\theta_H = 1$. Better agreement is observed between the predictions and experiment at measurement heights D and F than at measurement height B. This is again a result of the somewhat slower progression of the numerically determined melt front. A closer examination of the experimental data reveals that the temperatures at height D reach a higher temperature than at height F, which indicates some heat loss through the top boundary. However, the heat loss is less pronounced at the lower Stefan number ($Ste_L = 0.0836$) than at $Ste_L = 0.3265$. Thus the $Ste_L = 0.0836$ case is recommended for validation of numerical models.

As noted in Section 2.1, an insulated boundary condition was assumed at a radial position of $r = R + \delta = 34.75$ mm ($\delta = 2.85$ mm is the thickness of the polycarbonate wall) in the acrylic base in the interests of ease of computation, despite the actual diameter extending to $r_B = 120.7$ mm. The validity of the assumed boundary condition is examined by comparing the experimentally and numerically predicted temperatures along the *upper surface* of the acrylic base (i.e., the lower boundary of the PCM domain), as shown for $Ste_L = 0.0836$ in Fig. 8. A significant non-uniformity caused by the influence of the hot side wall is observed in both the experimental and numerical results at the *upper surface* of the acrylic base, whereas a constant temperature is maintained at the *bottom surface* due to the presence of the active heat sink. The fair agreement between experiment and prediction supports the use of the known constant and uniform temperature θ_B on the *bottom surface* of the acrylic base as the boundary condition in numerical models as shown in Fig. 1b and discussed in Section 2.1.

The deviation noted in this section between the numerical and experimental results at higher $(SteFo)_L$ may be attributed to several factors: imperfect application of experimental conditions in the model, experimental errors and uncertainties, and inadequacies in the numerical approach. One source of error results from the extraction of wax during the melting process as discussed in Section 2.2 since the reduction in mass within the enclosure is not accounted for in the model. Furthermore, while an 18% expansion of the material would be expected during the melting process based on the volumetric expansion of *n*-eicosane during solid/liquid phase change [24], only about an 8% expansion appears to have actually occurred during the experiment, as estimated from the amount of wax withdrawn. This difference is attributed to air pockets formed in the solid wax during the solidification process. The lower mass in the enclosure due to void formation and reduction

Fig. 6. Comparisons of experimentally and numerically determined (a) melt front locations and (b) volumetric liquid fraction.

(a)

Fig. 8. Experimental and numerical comparison of the temperature of the upper surface of the acrylic base (the lower PCM domain boundary) for $Ste_L = 0.0836$.
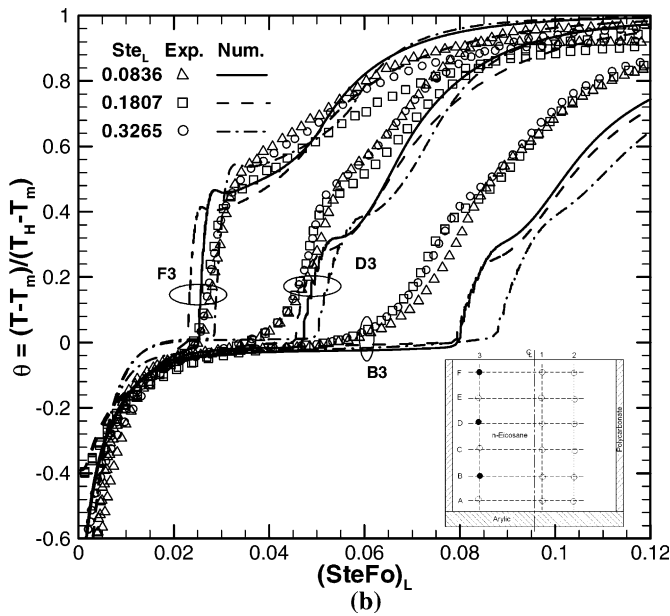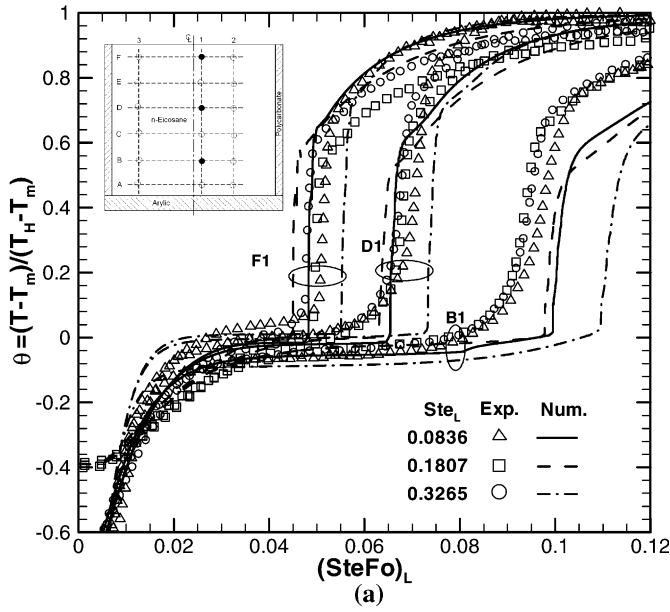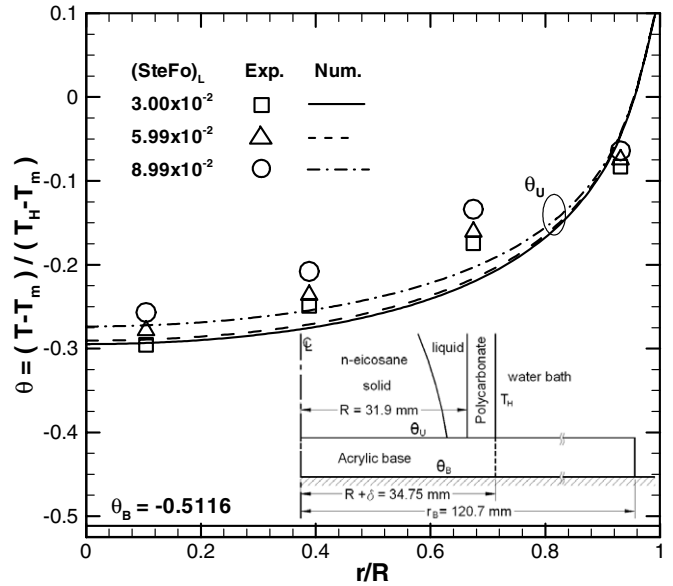

(b)

Fig. 7. Comparisons of numerically predicted and experimentally measured temperatures.

in mass due to wax removal was not considered in the model. The larger mass of wax imposed in the model may explain the somewhat slower melting predicted. Another source of error in the model results from the use of an adiabatic top boundary condition. As discussed in Section 2.1, there is finite heat loss through the top of the enclosure. This heat loss, however, would cause differences that partially offset the results of the other errors discussed above.

4.2.2. Heat transfer characteristics

Non-dimensional stream function contours and isotherms are shown in Fig. 9 for $Ste_L = 0.0836$. As discussed

in Section 4.1, the temperature distribution is initially dominated by conduction and a long narrow convection cell with $|\psi|_{max} = 15$ is observed (Fig. 9a). As melting progresses, the fluid velocities gradually increase, resulting in the formation of a more dominant and larger convective cell near the top of the cylinder and $|\psi|_{max}$ increases to 727 (Fig. 9b). The heat transfer at the bottom portion of the molten PCM, however, is still dominated by heat conduction, as indicated by the nearly parallel vertical isotherms. The average temperature of the bulk liquid continues to increase, which results in a decrease in the temperature gradient across the boundary layer along the inner sidewall (Fig. 9a–d). Once the melt front has reached the cylinder centerline, the two wall jets rising from the sidewall impinge at the centerline, leading to flow pattern changes at the top of the cylinder (Fig. 9c–d). The convection cell at the lower corner, where the largest temperature differences occur, remains strong during the entire melting process. It is noted that the isotherms in the acrylic base remain largely unchanged through much of the cycle. The contact area between the solid region and the bottom of the enclosure remains largely unchanged except near the end of the melting process. For example at $Ste_L = 0.0836$, the contact area starts to change only around $(SteFo)_L = 0.097$, while the PCM melts completely by $(SteFo)_L = 0.117$. Due to the relatively small Ra values in all three cases (see Table 2), only one counterclockwise convection cell was observed during almost the entire course of the melting and the cell increases in size as melting progresses.

The time histories of the computed area-averaged heat fluxes along both the side and bottom walls of the enclosure, where $q''_{side}(t) = \int q''_{r=R}(z,t)\,dz$ and $q''_{base}(t) = \int q''_{z=0}(r,t)r\,dr$, are shown in Fig. 10. The inner radius of the cylinder is designated R and $z = 0$ is the

(a) t = 1200 s, $|\psi|_{max}$ = 15

(b) t = 4800 s, $|\psi|_{max}$ = 727

(c) t = 8400 s, $|\psi|_{max}$ = 776

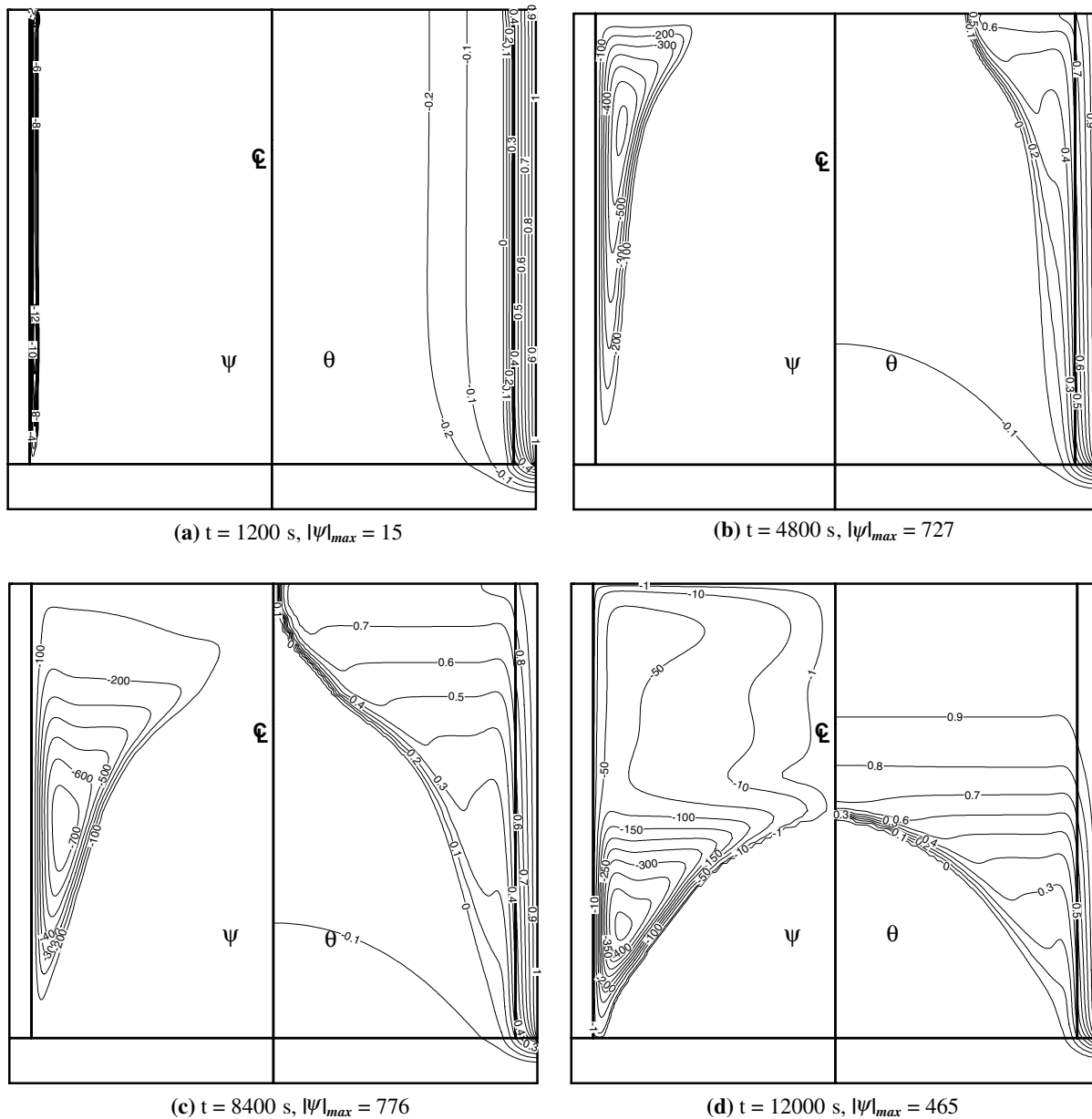**(d)** t = 12000 s, $|\psi|_{max}$ = 465

Fig. 9. Stream function (left) and temperature (right) contours for $Ste_L = 0.0836$ obtained using the numerical model.

bottom surface of the enclosure. Heat transfer to the PCM from the environment is taken to be positive. The heat fluxes through the bottom surface, in general, are approximately 5% of those through the sidewall. Early in the melting process, the bottom surface is warmer than the solid PCM; as a result, heat flows into the enclosure. As the temperature of the PCM increases and rises above the lower boundary temperature T_B, the heat flow direction changes. As seen in Fig. 7, the temperature of the solid wax at the bottom of the enclosure remains fairly constant after the initial temperature rise. Since the contact area of solid eicosane with the base also remains nearly constant through much of the experiment, q''_{base} remains relatively uniform after the initial heating. Towards the end of the melting process, the heat loss from the bottom starts to increase

as the PCM in contact with the base starts to melt. A larger Stefan number leads to a faster temperature rise in the bulk PCM due to greater contributions from sensible heating, and thus a more dramatic increase in q''_{base}.

Fig. 11 shows the average Nusselt number (base on the average amount of heat entering the cylindrical domain, $\overline{Nu} = \int_{z=0}^{H} k_S \frac{\partial T}{\partial r}\big|_{r=R^+} dz / \int_{z=0}^{H} k_L \frac{\partial T}{\partial r}\big|_{r=R^-} dz$ along the sidewall) as a function of non-dimensional time for three different Stefan numbers. Some of the features observed in Fig. 11 are similar to those for melting in a rectangular enclosure. Since the flow is laminar and $D/H > 35/(Ra_H/Pr)^{0.25}$ [37], the curvature effects can be neglected and the scaling analysis results reported in [36] can be extended to the current problem until the melt interface nears the axis of the cylinder. Once the front reaches the axis, the combined
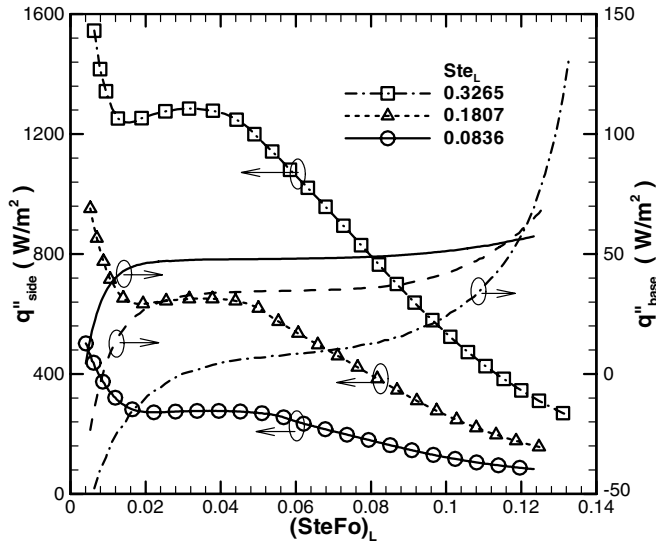
Fig. 10. Heat flux variations during the melting processes for different experimental conditions.
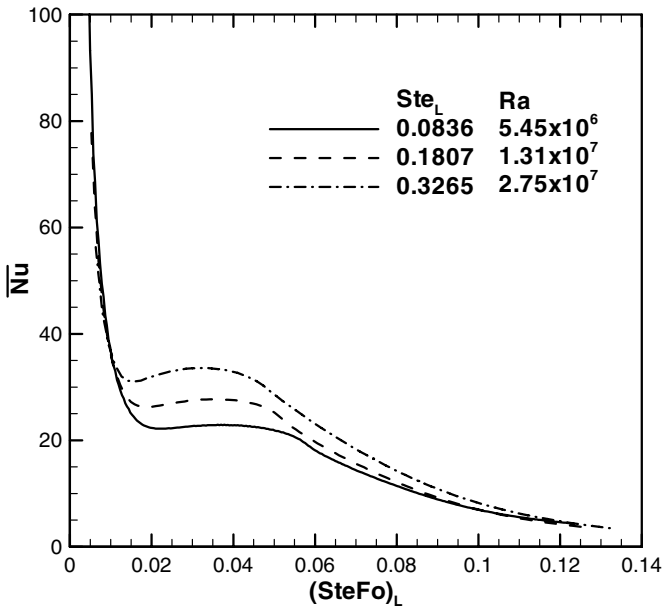

Fig. 11. Comparison of average Nusselt number along the sidewall at different cases.

effect of the cold temperature boundary on the bottom wall and the inward (impinging) radial flow due to natural convection significantly alters the melting process. Initially, at $(SteFo)_L = 0$, when the side-wall temperature is raised, heat transfer from the water bath to the PCM is large and is conduction-dominated. As the heat diffuses through the PCM, the Nusselt number falls rapidly as $\sim 2(SteFo)_L^{-1/2}$. As time progresses, $\overline{Nu}$ reaches a local minimum at a time scale $(SteFo)_L \sim O(36Ra_H^{-1/2})$ with a corresponding Nusselt number $\sim 0.2Ra_H^{0.25}$ [36]. This also corresponds to the beginning of the quasi-steady convective regime. The

variation in the different $\overline{Nu}$ curves is due to the differences in initial subcooling. Finally on a time scale $\sim O(4Ra_H^{-0.25})$, the melt front reaches the cylinder axis. The Nusselt number drops continuously from this point until the entire PCM is melted. As expected, there is no effect of Stefan number on the Nusselt number at the "steady state" and all curves converge to a natural convection limit (~ 4).

5. Conclusions

A well-controlled and well-characterized experimental study of the melting of subcooled n-eicosane in a cylindrical enclosure is conducted, complemented by a numerical investigation of the melting process. Experimental results include temperature measurements, solid/liquid interface locations, and volumetric liquid fractions. A semi-automated approach for extracting the solid/liquid interface locations using digital image processing techniques was developed. (A complete set of experimental results have been made available for public access through a website.) Comparisons between experimental measurements and numerical predictions for both melt front locations and temperature data reveal good general agreement, with the agreement being best at the lower Stefan numbers ($\leqslant 0.1807$). The experimental results for a Stefan number of 0.0836 are recommended for use in validation of numerical models. The melting process in the cylindrical enclosure is found to bear a resemblance to the four regimes developed by Jany and Bejan [36] for rectangular enclosures, i.e., conduction dominant, mixed convection/conduction, convection dominant and "shrinking solid" regimes.

Acknowledgements

References

[1] D. Sun, H. Zhang, J. Kalejs, B. Mackintosh, An advanced multi-block method for the multiresolution modelling of EFG silicon tube growth, Modell. Simul. Mater. Sci. Eng. 11 (2003) 83–90.

[2] S. Krishnan, S.V. Garimella, Thermal management of transient power spikes in electronics-phase change energy storage or copper heat sinks? ASME J. Electron. Packag. 126 (2004) 308–316.

[3] S. Krishnan, S.V. Garimella, Analysis of a phase change energy storage system for pulsed power dissipation, IEEE Trans. Compon. Packag. Technol. 27 (2004) 191–199.

[4] D. Sun, S.V. Garimella, S.K. Singh, N. Naik, Numerical and experimental investigation of the melt casting of explosives, Propell. Explos. Pyrot. 30 (2005) 369–380.

[5] J.O.M. Karlsson, E.G. Cravalho, M. Toner, A model of diffusion-limited ice growth inside biological cells during freezing, J. Appl. Phys. 75 (1994) 4442–4455.

[6] L.S. Yao, J. Prusa, Melting and freezing, Adv. Heat Transfer 19 (1989) 1–95.

[7] F. Wolff, R. Viskanta, Solidification of a pure metal at a vertical wall in the presence of liquid superheat, Int. J. Heat Mass Transfer 31 (1988) 1735–1744.

[8] C. Gau, R. Viskanta, Melting and solidification of a pure metal on a vertical wall, ASME J. Heat Transfer 108 (1986) 174–181.

[9] T.A. Campbell, J.N. Koster, Visualization of liquid–solid interface morphologies in gallium subject to natural convection, J. Cryst. Growth 140 (1994) 414–425.

[10] C.-J. Ho, R. Viskanta, Inward solid–liquid phase-change heat transfer in a rectangular cavity with conducting vertical walls, Int. J. Heat Mass Transfer 27 (1984) 1055–1065.

[11] C. Bénard, D. Gobin, F. Martinez, Melting in rectangular enclosures: experiments and numerical simulations, ASME J. Heat Transfer 107 (1985) 794–803.

[12] M. Bareiss, H. Beer, Influence of natural convection on the melting process in a vertical cylindrical enclosure, Lett. Heat Mass Transfer 7 (1980) 329–338.

[13] E.M. Sparrow, J.A. Broadbent, Freezing in a vertical tube, ASME J. Heat Transfer 105 (1983) 217–225.

[14] E.M. Sparrow, J.A. Broadbent, Inward melting in a vertical tube which allows free expansion of the phase-change medium, ASME J. Heat Transfer 104 (1982) 309–315.

[15] A.S. Menon, M.E. Weber, A.S. Majumdar, The dynamics of energy storage for paraffin wax in a cylindrical container, Can. J. Chem. Eng. 61 (1983) 647–653.

[16] A.D. Brent, V.R. Voller, K.J. Reid, Enthalpy-porosity technique for modeling convection–diffusion phase change: application to the melting of a pure metal, Numer. Heat Transfer 13 (1988) 297–318.

[17] J.E. Simpson, S.V. Garimella, An investigation of solutal, thermal and flow fields in unidirectional alloy solidification, Int. J. Heat Mass Transfer 41 (1998) 2485–2502.

[18] H. Zhang, V. Prasad, M.K. Moallemi, Numerical algorithm using multizone adaptive grid generation for multiphase transport processes with moving and free boundaries, Numer. Heat Transfer, Part B: Fundam. 29 (1996) 399–421.

[19] C.-J. Kim, M. Kaviany, A numerical method for phase-change problems with convection and diffusion, Int. J. Heat Mass Transfer 35 (1992) 457–467.

[20] R. Viswanath, Y. Jaluria, A comparison of different solution methodologies for melting and solidification problems in enclosures, Numer. Heat Transfer, Part B: Fundam. 24 (1993) 77–105.

[21] O. Bertrand, B. Binet, et al., Melting driven by natural convection. A comparison exercise: first results, Int. J. Therm. Sci. 38 (1999) 5–26.

[22] N. Hannoun, V. Alexiades, T.Z. Mai, Resolving the controversy over tin and gallium melting in a rectangular cavity heated from the side, Numer. Heat Transfer, Part B: Fundam. 44 (2003) 253–276.

[23] J.A. Dantzig, Modelling liquid–solid phase changes with melt convection, Int. J. Numer. Methods Eng. 28 (1989) 1769–1785.

[24] M. Frenkel, TRC Thermodynamic Tables—Hydrocarbons, US Government Printing Office, Washington, 2003.

[25] J.F. Shackelford, W. Alexander, J.S. Park, Practical Handbook of Materials Selection, CRC Press, Boca Raton, 1995.

[26] P.C. Stryker, E.M. Sparrow, Application of a spherical thermal conductivity cell to solid n-eicosane paraffin, Int. J. Heat Mass Transfer 33 (1990) 1781–1793.

[27] J. Brandrup, E.H. Immergut, E.A. Grulke, Polymer Handbook, John Wiley & Sons, New York, 1999.

[28] J. Timmermans, Physico-Chemical Constants of Pure Organic Compounds, Elsevier Publishing Company, Amsterdam, 1965, p. 57.

[29] MATLAB: The Language of Technical Computing, version 6.5, The MathWorks, Inc., Natick, MA, 2002.

[30] J.S. Lim, Two-Dimensional Signal and Image Processing, Prentice-Hall, Englewood Cliffs, 1990, pp. 478–483.

[31] C.L. Yaws, Chemical Properties Handbook, McGraw-Hill, New York, 1999.

[32] S. Himran, A. Suwono, G.A. Mansoori, Characterization of alkanes and paraffin waxes for application as phase change energy storage medium, Energy Sour. 16 (1994) 117–128.

[33] C.T. Lynch, Practical Handbook of Materials Science, CRC Press, Boca Raton, 1989.

[34] J. Ferziger, M. Peric, Computational Methods for Fluid Dynamics, Springer, 1999.

[35] C.D. Sulfredge, L.C. Chow, K.A. Tagavi, Solidification void formation for cylindrical geometries, Exp. Heat Transfer 3 (1990) 257–268.

[36] P. Jany, A. Bejan, Scaling theory of melting with natural convection in an enclosure, Int. J. Heat Mass Transfer 31 (1988) 1221–1235.

[37] A. Bejan, A.D. Kraus, Heat Transfer Handbook, John Wiley & Sons, New York, 2003.